Annu. Rev. Mater. Res. 2002. 32:163–94
doi: 10.1146/annurev.matsci.32.101901.155803

PHASE-FIELD SIMULATION OF SOLIDIFICATION[1]

W. J. Boettinger,[1] J. A. Warren,[1] C. Beckermann,[2] and A. Karma[3]

[1]*Metallurgy Division, Materials Science and Engineering Laboratory, NIST, Gaithersburg, Maryland 20899; e-mail: wboettinger@nist.gov; james.warren@nist.gov*
[2]*Department of Mechanical and Industrial Engineering, University of Iowa, Iowa City, Iowa 52242; e-mail: becker@engineering.uiowa.edu*
[3]*Department of Physics and Center for Interdisciplinary Research on Complex Systems, Northeastern University, Boston, Massachusetts 02115; e-mail: a.karma@neu.edu*

Key Words solid-liquid phase change, diffuse interface, microstructure, diffusion, convection

■ **Abstract** An overview of the phase-field method for modeling solidification is presented, together with several example results. Using a phase-field variable and a corresponding governing equation to describe the state (solid or liquid) in a material as a function of position and time, the diffusion equations for heat and solute can be solved without tracking the liquid-solid interface. The interfacial regions between liquid and solid involve smooth but highly localized variations of the phase-field variable. The method has been applied to a wide variety of problems including dendritic growth in pure materials; dendritic, eutectic, and peritectic growth in alloys; and solute trapping during rapid solidification.

INTRODUCTION

The formation of complex microstructures during solidification of metals and alloys and the accompanying diffusion and convection processes in the liquid and solid have fascinated researchers in materials science and related areas for literally hundreds of years. Examples include the growth of dendrites and eutectics (1–4) and microsegregation that occurs during growth (5–6). The principal obstacle in predicting solidification patterns is in accurately calculating the diffusion and convection processes in the liquid and solid for the complex shapes of the solid-liquid interface. Over the past few years, largely because of the development in a modeling approach called the phase-field method and ever-increasing computation power, much progress has been made in simulating solidification on the scale of the developing microstructure.

[1]The US Government has the right to retain a nonexclusive, royalty-free license in and to any copyright covering this paper.

Herein we give only an introduction to the phase-field modeling approach, because this field has recently exploded and a complete review is impossible in this short chapter. The subject now incorporates a variety of topics ranging from solidification, strain-accommodating solid-state transformations, and surface diffusion. The method employs a phase-field variable, e.g., ϕ, which is a function of position and time, to describe whether the material is liquid or solid. The behavior of this variable is governed by an equation that is coupled to equations for heat and solute transport. Interfaces between liquid and solid are described by smooth but highly localized changes of this variable between fixed values that represent solid and liquid, (in this review, 0 and 1, respectively).

This approach avoids the mathematically difficult problem of applying boundary conditions at an interface whose location is part of the unknown solution (the so-called Stefan problem). These boundary conditions are required so that the individual solutions to transport equations in the bulk phases match properly at the interface; i.e., conserve heat and solute and obey thermodynamic/kinetic constraints. In phase-field calculations, boundary conditions at the interface are not required. The location of the interface is obtained from the numerical solution for the phase-field variable at positions where $\phi = \frac{1}{2}$. The phase-field method is also powerful because it easily treats topology changes such as coalescence of two solid regions that come into close proximity.

Phase-field models can be divided into various intersecting classes: those that involve a single scalar order parameter and those that involve multiple order parameters; those derived from a thermodynamic formulation and those that derive from geometrical arguments. There are also formulations best suited for large deviations from local equilibrium and others for the opposite. There are physical problems where the order parameter can easily be associated with a measurable quantity such as a long-range chemical or displacive order parameter in solids and those where the order parameter is not easily measurable such as in solidification. In some cases, the method might represent real physics and in others, the method might be better viewed as a computational technique. Indeed, neither phase-field models nor sharp-interface models perfectly represent physical systems. In addition, phase-field models for solidification coupled to fluid flow are also being developed. This research should have a major impact on our understanding of flow in the mushy zone caused by shrinkage and buoyancy-driven convection.

THE PHASE-FIELD VARIABLE

A single, scalar order parameter can be used to model solidification of a single-phase material. However, to employ such a simple description of the liquid-solid transition necessarily requires a number of approximations. Figure 1 [adapted from Mikheev & Chernov (7)] shows one possible physical interpretation of a single scalar phase-field variable. The interfacial region and its motion during solidification are depicted by a damped wave that represents the probability of

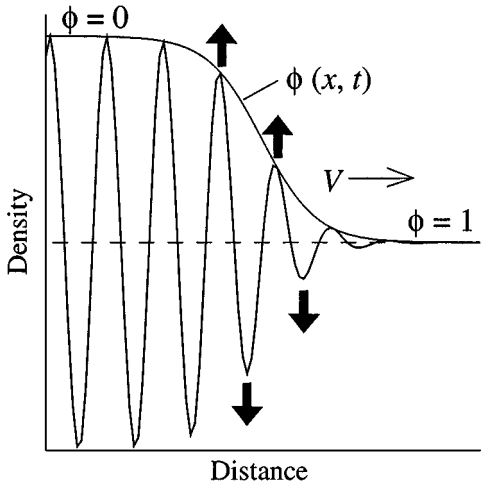

Figure 1 Schematic representation of a possible physical interpretation of the phase-field variable. [Adapted from Meekhev & Chernov (7).]

finding an atom at a particular location. On the left (Figure 1), the atoms tend to be located at discrete atomic planes corresponding to the crystal. As the liquid is approached, the probability has the same average value but becomes less localized, as indicated by the reduced amplitude of the wave. Finally the probability achieves a constant value in the liquid indicating the absence of localization of atoms to specific sites; i.e., a liquid. The amplitude of the wave might be related to the phase field ϕ.

For many solid-solid transformations, a set of order parameters naturally arises from the symmetry and orientation relationships between the phases. However, a rigorous description of the liquid-to-solid transformation requires an infinite number of order parameters. Starting with a representation of the atomic density variation across an interface in reciprocal space, Harrowell & Oxtoby (8) and Khachaturyan (9) described the approximations necessary to reduce the infinite number of order parameters to just one scalar. One can imagine the lattice of the crystal extending into the interfacial region. A Fourier series can be used to represent the local atomic density at each location.

The Fourier coefficients in the series are functions of distance. These functions are assumed to vary slowly (compared with the lattice spacing) through the interfacial region. For example in the one-dimensional schematic representation of Figure 1, a single wavelength sine wave is depicted with a slowly varying modulation amplitude. On the scale of the lattice spacing in this example, the amplitudes of the Fourier coefficients are approximately constant, and the density is spatially periodic with the period of the lattice. However, a detailed description of the density on this scale would require a full Fourier series containing other sine

waves with shorter wavelengths, each with slowly varying amplitudes that may vary differently through the interface, and hence an infinite set of order parameters (8, 9).

To reduce the full description to a single phase-field variable, two simplifying assumptions are necessary. The first assumes that the amplitudes associated with the interatomic spacings (shortest reciprocal lattice vectors) respond to interface motion most slowly; i.e., their adjustment limits the rate of crystal growth. Amplitudes associated with shorter wavelengths, it is argued, respond more quickly. Then the description of the liquid-to-crystal transition can be reduced to a small number of amplitudes that simply describe the probability of the occupancy at the lattice positions in the three-dimensional unit cell. The second simplification comes if one assumes that the amplitudes of this limited set of Fourier components are proportional to each other. Then a single scalar can describe the amplitudes as they vary across the interface, as in Figure 1. Such a description is most appropriate for metallic systems.

This second assumption eliminates the possibility of describing anisotropy in a physical way. Interface energies are rendered isotropic. For single-variable phase-field models, anisotropy must be introduced ad hoc through an orientation dependence of the gradient energy coefficients, as shown below. Alternatively, one can keep the multiple-order parameter picture and naturally derive anisotropy (10).

If one accepts that a single-order parameter can represent the transformation from liquid to a specified solid phase, then multiple scalar phase-field variables can be used to treat situations where more than two solid phases appear, e.g., eutectic and peritectic reactions. Multiple phase-field variables can also be used to treat the multiple orientations found in a polycrystalline material (11).

From a purely mathematical point of view the phase-field parameter can be considered a tool that allows easier calculations of solidification patterns. Mathematicians refer to this as a regularization of sharp interface problems. The sharp-interface solution is called a weak solution in that it satisfies the solute and heat transport field equations in an integrated form. The only mathematical requirement to support a smooth but rapidly changing function that represents an interface is a balance between two effects: an increase in energy associated with states intermediate between liquid and solid and an energy cost associated with large values of the gradient of the phase-field variable.

DIFFERENT PHASE-FIELD MODELS

There are two approaches to phase-field modeling: those that use a thermodynamic treatment with gradient flow and those that are only concerned with reproducing the traditional sharp-interface approach. In this section, we examine three cases of the above: (*a*) a thermodynamic treatment with a single scalar order parameter, (*b*) a practical or geometrical method with a single scalar order parameter where the equations are derived backward from the sharp-interface model, and

(*c*) a treatment with multiple phase-field parameters. We describe the first case in some detail, and briefly describe the others. The reader will note the similarities of the end result of the various approaches, each of which gives a different perspective.

Thermodynamic Treatment

This approach is found in many papers on the phase-field method (12–17) and determines the evolution equations from a few basic concepts of irreversible thermodynamics.

EVOLUTION EQUATIONS By demanding that the entropy always increases locally for a system where the internal energy and concentration are conserved, relationships between the fluxes of internal energy and concentration can be obtained. These are generalizations of Fourier's and Fick's laws of diffusion. A separate relationship governing ϕ is required to guarantee that the entropy increases.

To treat cases containing interfaces, the entropy functional S is defined over the system volume V as

$$S = \int_V \left[s(e, c, \phi) - \frac{\varepsilon_e'^2}{2}|\nabla e|^2 - \frac{\varepsilon_c'^2}{2}|\nabla c|^2 - \frac{\varepsilon_\phi'^2}{2}|\nabla \phi|^2 \right] dV, \qquad 1.$$

where s, e, c, and ϕ are the entropy density, internal energy density, concentration and phase field, respectively, with ε_e', ε_c' and ε_ϕ' being the associated gradient entropy coefficients. The entropy density s must contain a double well in the variable ϕ that distinguishes the liquid and solid. The quantity S also includes the entropy associated with gradients (interfaces). From such an approach, equations for energy (heat) diffusion, solute diffusion and phase field evolution follow naturally. The formulation using this entropy functional, especially with all three gradient energy contributions (17), is quite general.

We present a simpler isothermal formulation to which we append a heat flow equation. This gives essentially equivalent results to the entropy formulation if $\varepsilon_e' = 0$. The enthalpy density is expressed as

$$h = h_0 + C_P\, T + L\phi, \qquad 2.$$

which yields an equation for thermal diffusion with a source term given by

$$C_P \frac{\partial T}{\partial t} + L \frac{\partial \phi}{\partial t} = \nabla \cdot (k \nabla T), \qquad 3.$$

where h_0 is a constant; T is the temperature; C_p is the heat capacity per unit volume, which in general depends on temperature; L is the latent heat per unit volume; and k is the thermal conductivity. From the differential equation it can be seen that the latent heat evolution occurs where ϕ is changing with time, i.e., near a moving interface.

An isothermal treatment forms the free energy functional F, which must decrease during any process, as

$$F = \int_V \left[f(\phi, c, T) + \frac{\varepsilon_C^2}{2} |\nabla c|^2 + \frac{\varepsilon_\phi^2}{2} |\nabla \phi|^2 \right] dV, \quad 4.$$

where $f(\phi, c, T)$ is the free energy density, and where the gradient energy coefficients have different units than the (primed) gradient entropy coefficients used in Equation 1.

For equilibrium, the variational derivatives of F must satisfy the equations,

$$\frac{\delta F}{\delta \phi} = \frac{\partial f}{\partial \phi} - \varepsilon_\phi^2 \nabla^2 \phi = 0, \quad 5.$$

$$\frac{\delta F}{\delta c} = \frac{\partial f}{\partial c} - \varepsilon_C^2 \nabla^2 c = \text{constant} \quad 6.$$

if the gradient energy coefficients are constants. The constant in Equation 6 occurs because the total amount of solute in the volume V is a constant; i.e., concentration is a conserved quantity.

For time-dependent situations, the simplest equations that guarantee a decrease in total free energy with time (an increase in entropy in the general formulation) are given by

$$\frac{\partial \phi}{\partial t} = -M_\phi \left[\frac{\partial f}{\partial \phi} - \varepsilon_\phi^2 \nabla^2 \phi \right], \quad 7.$$

$$\frac{\partial c}{\partial t} = \nabla \cdot \left[M_C c(1-c) \nabla \left(\frac{\partial f}{\partial c} - \varepsilon_C^2 \nabla^2 c \right) \right]. \quad 8.$$

The parameters M_ϕ and M_C are positive mobilities related to the interface kinetic coefficient and solute diffusion coefficient, respectively, as described below. Equations 7 and 8 have different forms because composition is a conserved quantity and the phase field is not. Equation 7 is called the Allen-Cahn equation; Equation 8 is the Cahn-Hilliard equation. In this formulation, the pair are coupled through the energy function $f(\phi, c, T)$. In Equation 8, we set $\varepsilon_C = 0$ for the remainder of this review. With $\varepsilon_C \neq 0$ and a double well in $f(c)$, Equation 8 alone can describe spinodal decomposition.

FREE ENERGY FUNCTION The free energy density uses two functions: a double-well function and an interpolating function. Here we chose the two functions, $g(\phi) = \phi^2(1-\phi)^2$ and $p(\phi) = \phi^3(6\phi^2 - 15\phi + 10)$, respectively. Note that by design, $p'(\phi) = 30g(\phi)$, ensuring that $\partial f/\partial \phi = 0$ when $\phi = 0$ and 1, for all temperatures, as shown below. In this review, $\phi = 0$ represents solid and $\phi = 1$ represents liquid, although the opposite convention is often used. Plots of these functions are given in Figure 2.

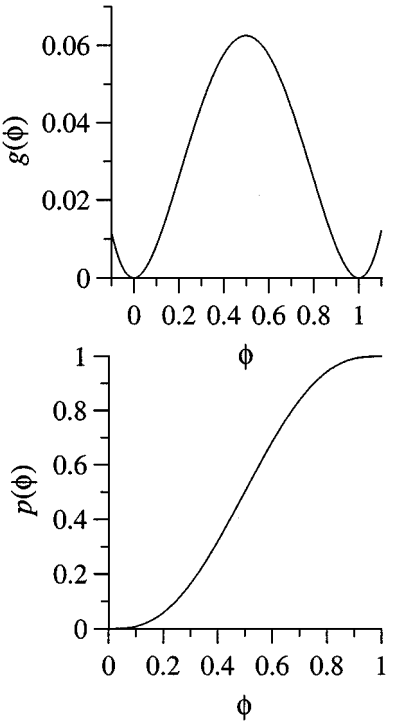

Figure 2 The functions $g(\phi)$ and $p(\phi)$.

The alloy free energy density $f(\phi, c, T)$ can be constructed in several ways. One method can be broken into three steps:

1. Start with the ordinary free energy of the pure components as liquid and solid phases, $f_A^L(T)$, $f_A^S(T)$, $f_B^L(T)$ and $f_B^S(T)$. They are functions of temperature only.
2. Form a function, $f_A(\phi, T)$, that represents both liquid and solid for pure A as

$$\begin{aligned} f_A(\phi, T) &= (1 - p(\phi))\, f_A^S(T) + p(\phi)\, f_A^L(T) + W_A g(\phi) \\ &= f_A^S + p(\phi)\left[f_A^L(T) - f_A^S(T)\right] + W_A g(\phi). \end{aligned} \tag{9.}$$

   This function combines the free energies of the liquid and solid with the interpolating function $p(\phi)$ and adds an energy hump, W_A, between them. A similar expression can be obtained for component B here and in all expressions below for a pure substance.
3. Form the function, $f(\phi, c, T)$, that represents (for example) a regular

solution of A and B,

$$f(\phi, c, T) = (1-c)\, f_A(\phi, T) + c f_B(\phi, T) + R'T\,[(1-c)\ln(1-c) + c\ln c] + c(1-c)\,\{\Omega_S\,[1-p(\phi)] + \Omega_L\, p(\phi)\}, \quad 10.$$

where Ω_L and Ω_S are the regular solution parameters of the liquid and solid that again are combined with the interpolating function $p(\phi)$. The gas constant R' and the regular solution parameters are described on a unit volume basis.

A second method to form $f(\phi, c, T)$ is convenient if the free energies of the solid phase and liquid phase, $f^L(c, T)$ and $f^S(c, T)$, are already available; e.g., from a Calphad thermodynamic modeling of the phase diagram. The free energy density is

$$f(\phi, c, T) = [(1-c)\, W_A + c W_B]\, g(\phi) + [(1-p(\phi)]\; f^S(c, T) + p(\phi) f^L(c, T). \quad 11.$$

Such a construction will lead to the same form as Equation 10 if regular solution models are used for the liquid and solid phases.

A simplification is often made for the pure elements; namely,

$$f_S^A(T) = 0$$
$$f_L^A(T) - f_S^A(T) = \frac{L\left(T_M^A - T\right)}{T_M^A}. \quad 12.$$

This takes the solid as the standard state and expands the difference between liquid and solid free energies around the melting point. The pure component melting points are T_M^A and T_M^B, and the latent heats are L_A and L_B. Then the pure element free energy (Equation 9) can be given by

$$f_A(\phi, T) = W_A g(\phi) + L_A \frac{T_M^A - T}{T_M^A} p(\phi). \quad 13.$$

The effect of the second term is to raise or lower the minimum in the free energy at $\phi = 1$ (liquid) depending on the whether the temperature is above or below the melting point with the free energy at $\phi = 0$ (solid) being fixed at zero.

The choice for the form of the functions $g(\phi)$ and $p(\phi)$ is arbitrary and others are used in various publications. In the limit in which the interface thickness is small, the choice does not matter.

SOLUTIONS FOR A PURE MATERIAL Consider the case where $c = 0$; i.e., pure component A. From Equations 7 and 13,

$$\frac{\partial \phi}{\partial t} = M_\phi^A \varepsilon_\phi^2 \left[\nabla^2 \phi - \frac{2W_A}{\varepsilon_\phi^2} \phi(1-\phi)(1-2\phi) \right] - \frac{30 M_\phi^A L_A}{T_M^A} \left(T_M^A - T\right) \phi^2 (1-\phi)^2. \quad 14.$$

Equilibrium solutions ($\partial\phi/\partial t = 0$) are obtained if ϕ is constant with values equal to 0 or 1. These situations correspond to a single-phase solid or a single-phase liquid, respectively. The equilibrium equation (Equation 5) permits these states to exist at any temperature, including those for a metastable supercooled liquid or a superheated solid.

An equilibrium solution also exists at $T = T_M^A$ for a one-dimensional (planar interface) transition zone between liquid ($\phi = 1$) and solid ($\phi = 0$) where ϕ varies in the x direction normal to the interface as

$$\phi(x) = \frac{1}{2}\left[1 + \tanh\left(\frac{x}{2\delta_A}\right)\right], \quad 15.$$

where δ_A is a measure of the interface thickness given by

$$\delta_A = \frac{\varepsilon_\phi}{\sqrt{2W_A}}. \quad 16.$$

The value of the interface thickness is a balance between two opposing effects. The interface tends to be sharp in order to minimize the volume of material where ϕ is between 0 and 1 and $f(\phi, T)$ is large (as described by W_A). The interface tends to be diffuse to reduce the energy associated with the gradient of ϕ (as described by ε_ϕ).

Figure 3 shows the variation of ϕ and the integrand of Equation 4, $f(\phi, T_M) + \frac{1}{2}\varepsilon_\phi^2 |\nabla\phi|^2$, with distance across an interfacial region for the equilibrium solution (Equation 15). The hatched region corresponds to the surface free energy and is given by direct integration using Equation 15 as

$$\sigma_A = \frac{\varepsilon_\phi \sqrt{W_A}}{3\sqrt{2}}. \quad 17.$$

Note that it is possible to take the limit, $\delta_A \to 0$, while keeping σ fixed. Equations 16 and 17 can be used to calculate the values of the parameters ε_ϕ and W_A to match with selected values for σ_A and δ_A; namely,

$$\varepsilon_\phi = \sqrt{6\sigma_A \delta_A} \quad \text{and} \quad W_A = 3\frac{\sigma_A}{\delta_A}. \quad 18.$$

For the planar solution, the Laplacian, $\nabla^2\phi$, is simply the second derivative of ϕ wrt. x. To examine a curved equilibrium interface (Equation 14 with $\partial\phi/\partial t = 0$), the simplest mathematics is to transform to spherical coordinates with no angular dependence. Then the Laplacian includes an extra term, in addition to the second

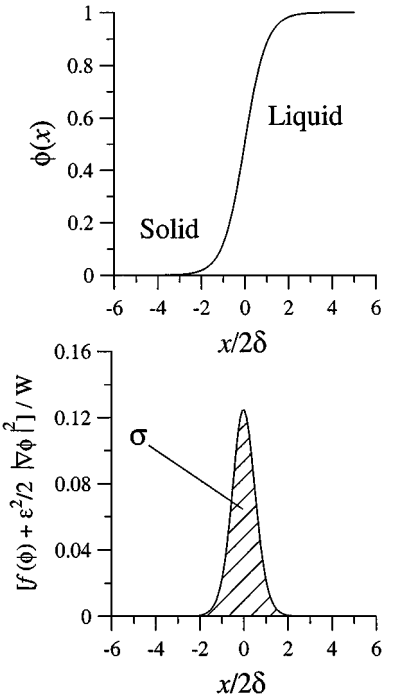

Figure 3 Variation of the phase-field parameter, ϕ, and the energy/unit volume, $f(\phi) + \frac{1}{2}\varepsilon_\phi^2(\nabla\phi)^2$, with distance, x, across a stationary flat liquid-solid interface at the melting point in a pure material. The area under the curve in the latter is the excess energy/unit area of interface, i.e., the liquid-solid interface energy.

derivative wrt. r ; i.e., $(2/r)(\partial\phi/\partial r)$. With this extra term, no solution exists when $T = T_M^A$. However, for an interface with a specified radius, $R \gg \delta_A$, a solution does exist at a temperature below T_M^A; that is, $T = T_M^A - \Gamma/R$, where $\Gamma = \sigma T_M^A/L_A$. This selection of one interface radius for each (interface) temperature is consistent with the Gibbs-Thomson effect for a sharp-interface model.

To examine a moving, flat steady-state interface, the simplest mathematics is to transform Equation 14 in one dimension to a coordinate frame moving at constant velocity v. Then $\partial\phi/\partial t$ changes to $-v(\partial\phi/\partial x)$. With this change, no solution exists if $T = T_M^A$. However, a solution does exist for small δ_A if the temperature is given by

$$T = T_M^A - \frac{v}{\mu_A}, \tag{19.}$$

where

$$\mu_A = \frac{6M_\phi\varepsilon_\phi L_A}{T_M^A\sqrt{2W_A}}. \tag{20.}$$

The selection of one interface velocity for each (interface) temperature is consistent with the classical approach to linear interface attachment kinetics. Equation 20 can be used to determine a value of M_ϕ^A from a knowledge (or estimate) of μ_A as

$$M_\phi^A = \frac{\mu_A T_M^A}{6\delta_A L_A}. \qquad 21.$$

In numerical solutions, the minimum mesh spacing must scale with the chosen value of δ_A so that the interface structure can be resolved. Physically for metallic systems, the interface thickness is of the order of a few atomic dimensions. Such a fine mesh spacing is only practical in one dimension at the current time. Thus one would prefer to use a larger value of δ and retain the accuracy of Equation 19. By treatment of the temperature variation that must exist across a diffuse interface, Karma & Rappel (18) have calculated the relation between μ_A and M_ϕ^A that is correct to second order in δ_A (if the thermal conductivity of the liquid and solid are equal). In this approach, they determined that if the interface width is still small compared with the macroscale of the microstructural detail of interest, then (using our own notation)

$$\frac{1}{M_\phi^A} = \frac{6\delta_A L_A}{T_M^A}\left[\frac{1}{\mu_A} + A\left(\frac{\delta_A L_A}{k}\right)\right], \qquad 22.$$

where $A \approx 5/6$. As $\delta_A \to 0$, Equation 22 recovers Equation 21.

As pointed out by Karma & Rappel, if one wants to treat the case of local interface equilibrium where $\mu_A = \infty$, then for a given value of δ_A, Equation 22 gives the appropriate value of M_ϕ^A. This is useful because many researchers are interested in comparing the predictions of the phase-field method with mathematical solutions of the sharp-interface formulation that assume local equilibrium (i.e., ignoring interface kinetics). On the other hand, some researchers are interested in high solidification speed where interface kinetics plays a very important role. Indeed, an example given below shows how the phase field method can recover the phenomenon of solute trapping for alloy solidification at high velocity.

ANISOTROPY, NOISE, AND NUMERICAL CONSIDERATIONS FOR SIMULATION OF DENDRITIC GROWTH To obtain realistic simulations of dendrites using the phase-field equations, three other issues must be addressed: anisotropy, noise, and computation times. The most widely used method to include anisotropy for two-dimensional calculations is to assume that ε_ϕ in Equation 4 depends on an angle θ (19). Here θ is the orientation of the normal to the interface with respect to the x-axis given by $\tan\theta = (\partial\phi/\partial y)/(\partial\phi/\partial x)$. This change requires a recomputation of the variational derivative in Equation 5, resulting in a more complex field equation for ϕ. Using this method of including anisotropy, formal asymptotics, as the interface thickness is taken to zero, yields the same form of the anisotropic Gibbs-Thompson equation that is employed for sharp-interface theories (20). For numerical computations of cubic dendrites in two dimensions,

fourfold variations of ε with θ have been utilized (19). Methods for including anisotropy in three-dimensions have also have been developed.

Calculations performed using a coarse, finite-difference mesh will usually exhibit side branching typical of real dendrites because discretization errors introduce noise into the calculation. (A coarse, square mesh can also induce a synthetic fourfold anisotropy). As the computational mesh is refined, however, side branches disappear. Therefore, to study realistic structures, noise is introduced at controlled levels to induce side branching. This is typically implemented using random fluctuations of a source term added to the phase-field equation (19, 21).

Computational issues associated with solving the phase-field equations are challenging and have primarily focused on the value of the interface thickness and the finite-difference mesh spacing. The central difficulty is having sufficient numerical resolution of the diffuse interface and at the same time enough nodes/elements to model the entire dendritic structure, often limiting consideration to high supercooling. This is an active area of research. In particular, techniques using adaptive finite-element calculations have been useful for enabling more efficient simulations (22). Hybrid methods are also being developed that solve the thermal diffusion equation using random walkers rather than a numerical solution to the differential equation (23).

SOLUTIONS FOR ALLOYS We recall the general form of the free energy, $f(\phi, c, T)$ (Equation 10), for the case of an alloy. The general shape is shown in Figure 4*a* for $\Omega \leq 0$ and at a fixed temperature between the pure component melting points. For fixed temperature, simultaneous solution of Equations 5 and 6 in one dimension show that ϕ will vary from 1 to 0 across a stationary interface between liquid and solid as c varies between two specific compositions c_L and c_S, shown by the dotted line on the (ϕ, c) base of the plot. The values far from the interface are given by a plane tangent at two points to the free-energy surface. The tangent plane has the properties that

$$\frac{\partial f}{\partial \phi} = 0 \quad \text{and} \quad \frac{\partial f}{\partial c} = \text{constant} \qquad 23.$$

as required by Equations 5 and 6 whenever ϕ and c have no spatial variation; i.e., far from the interface. This construction is the same as that obtained by classical thermodynamic methods applied to equilibrium between bulk phases; namely, the common tangent construction to the liquid and solid free energies at the selected temperature. The common tangent line to $f(0, c, T)$ and $f(1, c, T)$ at fixed T is the projection of the tangent plane to the surface $f(\phi, c, T)$, as shown in Figure 4*b*.

Dynamic solutions are described below. The phase-field mobility and the diffusion mobility are given by

$$M_\phi = (1 - c)M_\phi^A + cM_\phi^B$$

$$M_C = \frac{[1 - p(\phi)]D_S + p(\phi)D_L}{R'T}, \qquad 24.$$

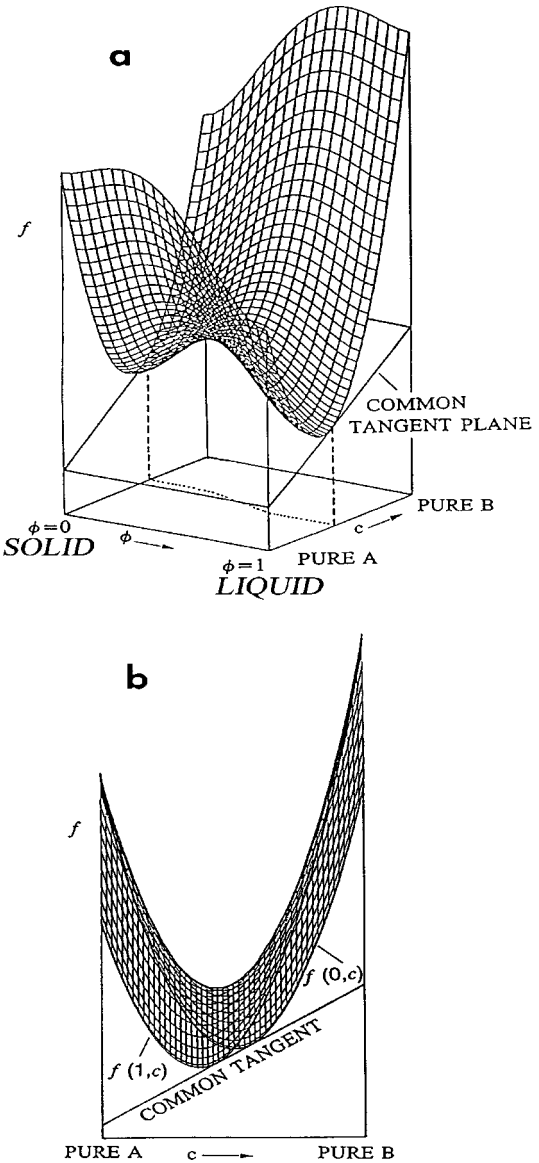

Figure 4 (*a*) The alloy free-energy function $f\ (\phi, c, T)$ for a temperature, T, between the pure component melting points ($T_M^B < T < T_M^A$), showing the tangent plane that determines the compositions of liquid and solid, far from a stationary flat interface. The locus of ϕ and c through the thin interfacial region is shown (*dotted line*). (*b*) Projection of (*a*) along the ϕ axis showing the common tangent line. The free-energy surface is only shown for $0 < \phi < 1$.

where D_L and D_S are the diffusion coefficients in the bulk liquid and solid phases. Also, we note that the interpolating function $p(\phi)$ need not be the same as the interpolating function introduced in Equation 9.

Karma (24) recently developed a modified phase-field formulation of alloy solidification that is designed to model quantitatively small solidification speeds under the assumption of local equilibrium at the interface, thereby generalizing Equation 22 to the alloy case. Moreover, as in the pure case, this formulation makes it possible to model this growth regime using a computationally tractable interface width in the phase-field model, i.e., a width that is substantially larger than the nanometer width of the real solid-liquid interface. For the alloy phase-field formulation discussed in the present review, the use of a large interface width generates nonequilibrium effects that are unrealistically large at small solidification speeds and that alter both the interface evolution and the solute profile in the solid.

Geometrical Description

Beckermann et al. (25) provide another approach for obtaining the phase-field equations. This approach also includes fluid flow, but here we present the case with no flow. If one considers the function $\phi(x, y, z, t)$ with the interface represented by a constant value of ϕ, then the normal to the interface n is given by

$$\vec{n} = \frac{\nabla\phi}{|\nabla\phi|}. \tag{25.}$$

The curvature κ is given by

$$\kappa = \nabla \cdot \vec{n} = \frac{1}{|\nabla\phi|}\left(\nabla^2\phi - \frac{\nabla\phi\nabla|\nabla\phi|}{|\nabla\phi|}\right). \tag{26.}$$

The normal velocity of the interface, v, is given by

$$v = -\frac{1}{|\nabla\phi|}\frac{\partial\phi}{\partial t}. \tag{27.}$$

The conditions for the liquid solid interface, written in the form where solute trapping is neglected, is

$$\frac{v}{\mu_A} = T_M^A - T + m_L c_L - \frac{\sigma T_M^A}{L_A}\kappa, \tag{28.}$$

where m_L is the liquidus slope. For a variation of ϕ in the normal direction n across the interface given by

$$\phi = \frac{1}{2}\left[1 + \tanh\left(\frac{n}{2\delta}\right)\right] \tag{29.}$$

one can compute

$$|\nabla\phi| = \frac{\partial\phi}{\partial n} = \frac{\phi(1-\phi)}{\delta} \tag{30.}$$

and

$$\frac{\nabla\phi\nabla|\nabla\phi|}{|\nabla\phi|} = \frac{\partial^2\phi}{\partial n^2} = \frac{\phi(1-\phi)(1-2\phi)}{\delta^2}. \quad 31.$$

Substituting the appropriate expressions into the interface equation yields

$$\frac{1}{\mu_A}\frac{\partial\phi}{\partial t} = \frac{\sigma_A T_M^A}{L_A}\left[\nabla^2\phi - \frac{\phi\,(1-\phi)(1-2\phi)}{\delta^2}\right] - (T_M - T + m_L c_L)\left[\frac{\phi(1-\phi)}{\delta}\right] \quad 32.$$

The concentration equation is derived by writing the following conservation equation using phase-field weighted values for the average concentration:

$$\frac{\partial c}{\partial t} = \nabla\cdot[(1-\phi)D_S\nabla c_S + \phi D_L\nabla c_L]\,. \quad 33.$$

The liquid and solid concentrations can be expressed in terms of the average concentration c as

$$c_L = \frac{c}{\phi + k(1-\phi)} \quad \text{and} \quad c_S = \frac{kc}{\phi + k(1-\phi)}, \quad 34.$$

where k is the solute partition coefficient. This method is particularly attractive if one does not wish to deal with the free energy functions to determine the phase diagram. Here, only the values of T_M^A, m_L and k are required. The method also provides a sense of the relationship between terms in the phase-field equation and quantities such as the interface curvature and velocity.

We note that if a different interpolation function, i.e., $p(\phi) = 3\phi^2 - 2\phi^3$, had been used in Equation 13 for the derivation of Equation 14, Equation 14 would be identical to Equation 32 for a pure material ($c_L = 0$).

Multiple Phase-Field Methods

Using a positive value of Ω_S in Equation 10, a solid miscibility gap can be formed in the binary phase diagram. In this case Figure 4 would add an energy hump along the concentration axis for the solid. The tangent plane would then have three tangent points corresponding to one liquid phase and two solid phases. In this manner and with $\varepsilon_C \neq 0$, multiphase problems such as eutectic and peritectic (monotectic with $\Omega_L \gg 0$) solidification problems can be examined (26). However it is not possible to represent all binary phase diagrams with the free energy of Equation 10. Therefore, it has become useful to use multiple phase-field variables to represent multiphase situations (26–28). The same general approach also allows the treatment of multiple grains (11), although it is argued that this approach imposes certain unphysical restrictions on the physics the model can describe (29).

The method begins by defining N variables ϕ_i, each of which is unity in the corresponding ith single phase region of the sample such that

$$\sum_{i=1}^{N} \phi_i = 1. \tag{35.}$$

Using our notation and definition of pure solid as the standard states, the free energy density is given by

$$f = \sum_{j,k(j<k)}^{N} \left\{ W_{jk} \left[\phi_j^2 \phi_k^2 - \frac{m_{jk}}{3} \left(1 + \phi_j^3 + 3\phi_j^2 \phi_k - 3\phi_j \phi_k^2 - \phi_k^3 \right) \right] \right\}, \tag{36.}$$

where W_{jk} is a symmetric matrix related to the double-well barrier heights for an interface between the jth and kth phases. The matrix m_{kj} is an antisymmetric matrix that describes the undercooling of each interface with respect to its equilibrium temperature. It is a function of T and c_L. In this form the energies associated with triple lines have been neglected. For alloys, this matrix can be derived from a full thermodynamic treatment, as in Nestler & Wheeler (30). Tiaden et al. (28) use a simpler method where

$$m_{ij} = \frac{3(h_i - h_j)\left(T - T_j^i\right)}{2W_{ij} T_i^j}, \tag{37.}$$

with h_i the enthalpy of the ith phase and T_i^j given by the phase diagram boundary between the ith and the (ith + jth) phase regions; e.g., T_L^S is the liquidus and T_S^L is the solidus.

The free energy functional is written as

$$F = \int_V \left\{ f(\phi_1, \ldots, \phi_N) + \sum_{j,k(j<k)}^{N} \left[\frac{\varepsilon_{jk}^2}{2} |\phi_j \nabla \phi_k - \phi_k \nabla \phi_j|^2 \right] \right\} dV, \tag{38.}$$

where ε_{jk} is the symmetric matrix of gradient energy coefficients. The dynamical response for isotropic interface energy is given by

$$\frac{\partial \phi_i}{\partial t} = \sum_{j=1(j\neq i)}^{N} M_{ij} \left[\varepsilon_{ij}^2 (\phi_j \nabla^2 \phi_i - \phi_i \nabla^2 \phi_j) - 2\phi_i \phi_j W_{ij} (\phi_j - \phi_i - 2m_{ij}) \right], \tag{39.}$$

where M_{ij} is the mobility of the i/j interface. Anisotropy is treated by changing the constants ε_{ij} into a function $\varepsilon_{ij}(\phi_i \nabla \phi_j - \phi_j \nabla \phi_i)$ in Equation 38 and recomputing the appropriate form of Equation 39. For only two phases, Equation 39 can recover Equation 14 by letting $\phi_1 = \phi$ and $\phi_2 = 1 - \phi$ and again using the interpolating function $p(\phi) = 3\phi^2 - 2\phi^3$. Transport equations for the concentration can be derived from a full thermodynamic treatment (30) or by using balance equations for an average concentration using the partition coefficients to define a phase-field-weighted sum of liquid and solid concentrations as done above.

To model different grains, one must select N grain orientations, the presence of which is described by an individual ϕ_i value (11). Another method (29) is being used that avoids the problem of a finite set of orientations.

Incorporation of Convection

Flow in the liquid phase is well documented to strongly influence microstructural evolution in solidification, and its dominant effect is to speed up the transport of heat or mass on large scales. Different means of incorporation of this effect into phase-field models have been developed. One is to treat the solid as a highly viscous liquid. This has been done by simply letting the viscosity depend on the phase field in the standard Navier-Stokes equations (31–33), or by deriving a thermodynamically consistent set of phase-field equations (34). The thermodynamic formulation is very general in that it includes the effects of density differences between the phases, viscous dissipation, and the dependence of the interface temperature on the pressure in the phases. A nonequilibrium form of the Clausius-Clapeyron equation was derived that includes the effects of curvature, attachment kinetics, and viscous dissipation.

Another method is to use the geometrical description (reviewed above) and view the diffuse interface region as a rigid porous medium, where the porosity is identified with the phase-field variable (25). In this method, the usual no-slip condition at a sharp solid-liquid interface is enforced through a varying interfacial force term in the diffuse interface region. The mass and momentum conservation equations can then be written, respectively, as

$$\nabla \cdot (\phi \vec{V}) = 0 \tag{40.}$$

and

$$\frac{\partial \phi \vec{V}}{\partial t} + \phi \vec{V} \cdot \nabla \vec{V} = -\phi/\rho \nabla P + \nu \nabla^2 (\phi \vec{V}) + \vec{M}_d, \tag{41.}$$

where $\vec{V}$, P, ρ, and ν are, respectively, the liquid velocity, pressure, density, and kinematic viscosity. All properties are assumed constant, and the densities of the solid and liquid phases are assumed equal. The last term in Equation 41 represents the dissipative interfacial force and is modeled as

$$\vec{M}_d = -\frac{\nu b (1-\phi)^2 \phi \vec{V}}{\delta^2}. \tag{42.}$$

This term acts as a spatially distributed momentum sink in the diffuse interface region that forces the liquid velocity to zero as $\phi \to 0$ (solid). The dimensionless constant $b = 2.757$ was determined by requiring that the velocity profile of the phase-field model coincides, away from the interface, with the profile near a sharp interface where the tangential component of $\vec{V}$ vanishes at $\phi = 0.5$. The main advantage of this approach is that accurate velocity profiles are obtained regardless of the diffuse interface thickness. In the presence of flow, phase-field-dependent

advection terms must also be added to the energy and species conservation equations (25). In Reference (25), the evolution equation for the phase-field variable was assumed to be the same as without flow, thus neglecting the dependence of the interface temperature on pressure.

EXAMPLES

Solute Trapping

Phase field models that are thermodynamically motivated have distinct advantages for certain types of investigations. One example is the insight gained on the phenomenon of solute trapping during solidification (35). One-dimensional steady-state calculations were performed for a dilute ideal solution alloy (lens-shaped phase diagram) with an equilibrium partition coefficient k_E of 0.8 and concentration 0.0717. Because the calculations are one-dimensional, grid resolution does not present a problem. The diffusion in the interface is described by Equation 24 with $D_S/D_L = 10^{-5}$, but with $p(\phi) = \phi$.

In a sharp-interface model with equilibrium interface conditions, as the velocity increases, the maximum concentration in the liquid at the interface remains at 0.09, and the length scale of the solute profiles in the liquid progressively shortens as D_L/V. For the phase-field model results (Figure 5), the solute profile at low velocity is similar to that given by the sharp-interface model. However, as the interface velocity increases, not only does the solute decay length diminish, but the maximum value of the solute concentration decreases as well. This reduction of the segregation of solute near the interfacial region indicates the presence of solute trapping. In contrast to the solute profiles shown in Figure 5, the corresponding $\phi(x)$ profiles are almost identical over this range of velocities.

For comparison of the phase-field numerical results with the Aziz dilute alloy-trapping model (36), we adopt a definition that the nonequilibrium partition coefficient is given by $k = c_\infty/c_{\max}$, where $c_{\max}$ is the maximum value of the concentration, and c_∞ is the concentration of the solid (or liquid) far from the interface. Numerical results for various values of dimensionless velocity are shown as the data points in Figure 6.

The dilute alloy Aziz solute-trapping model (36) for the velocity-dependent partition coefficient $k(V)$ is given by

$$k(V) = \frac{k_E + V/V_D}{1 + V/V_D}, \tag{43.}$$

where V_D is the characteristic trapping velocity. Comparing this equation to the phase-field model as $V \to \infty$, an expression for V_D is obtained (35),

$$V_D = \frac{3}{16}\left[1 + \frac{D_S}{D_L}\right]\left[\frac{\ln(1/k_E)}{(1-k_E)}\right]\left[\frac{D_L}{\delta}\right]. \tag{44.}$$

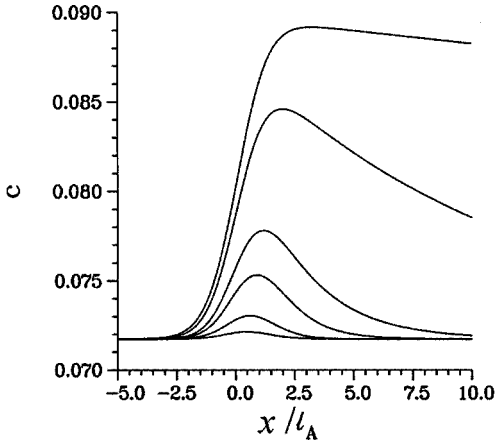

Figure 5 The computed solute profiles for six different values of the dimensionless interface velocity, $V\delta/D_L$, of (from the top curve to the bottom curve) 8.58×10^{-3}, 8.0×10^{-2}, 0.429, 0.859, 2.58, and 8.58. The solid composition is 0.0717, and the liquid concentration for local equilibrium is 0.09 ($k_E = 0.8$). $\ell_A = \delta$.

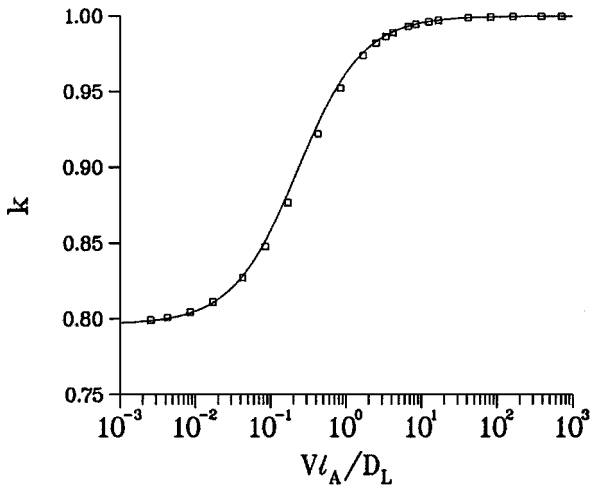

Figure 6 The squares denotes the values of the partition coefficient versus the normalized interface velocity $V\delta/D_L$ obtained from numerical computations with $D_S/D_L = 10^{-5}$. The solid curve shows the corresponding dependence of k on the interface velocity that is predicted by the Aziz model with V_D given by Equation 44, $\ell_A = \delta$.

Figure 6 shows a graph of Equation 43 for a value of V_D equal to $0.21D_L/\delta$ obtained from Equation 44 with $k_E = 0.8$, and $D_S/D_L = 10^{-5}$. An excellent description of the numerical results is obtained for solidification velocities ranging over six orders of magnitude. The dependence of V_D on k_E through Equation 44 was not previously predicted.

In Figure 7 we compare the experimental data for V_D obtained by Aziz (37) for both silicon and aluminum alloys to the quantity $\ln[k_E/(k_E - 1)]$. The correlation indicates that the model is in qualitative agreement with the experimental results, correctly predicting an increase in V_D with decreasing equilibrium partition coefficient.

Dendritic Growth

PURE SUBSTANCES Quantitative phase-field simulations of free (equiaxed) dendritic growth have been carried out in three dimensions at both low undercooling (assuming local equilibrium at the interface and using Equation 22) (18, 21, 23, 38) and at high undercooling with the incorporation of anisotropic interface kinetic effects (39). In both limits, phase-field simulations have been found to be in good quantitative agreement with the sharp-interface solvability theory of

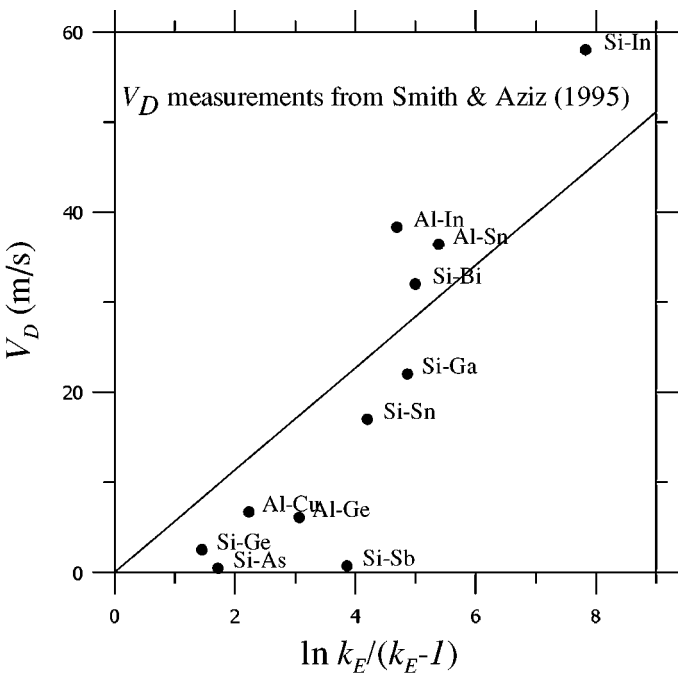

Figure 7 Experimental values for V_D (32) plotted versus the quantity $\ln[k_E/(k_E - 1)]$. The line is a linear fit through the origin.

dendritic growth (40, 41) in which the anisotropy of the interfacial energy and/or the interface kinetics (39) plays a crucial role in determining the steady-state operating state of the dendrite tip. This is illustrated for the low-undercooling limit in Figure 8 (38). In the high-undercooling limit, the phase-field simulations were carried out for Ni using as input interfacial properties computed from atomistic molecular dynamic simulations (42, 43). These phase-field simulations revealed that the interface dynamics are controlled sensitively by the magnitude of the kinetic anisotropy (39) and that dendrites cease to exist above a critical undercooling if this magnitude is too small.

EFFECTS OF CONVECTION Convective effects on dendritic growth have been studied by a number of investigators using the phase-field method (25, 31–33, 44–46). Figure 9 gives an example of a two-dimensional simulation of free dendritic growth into a supercooled melt, where the melt enters at the top

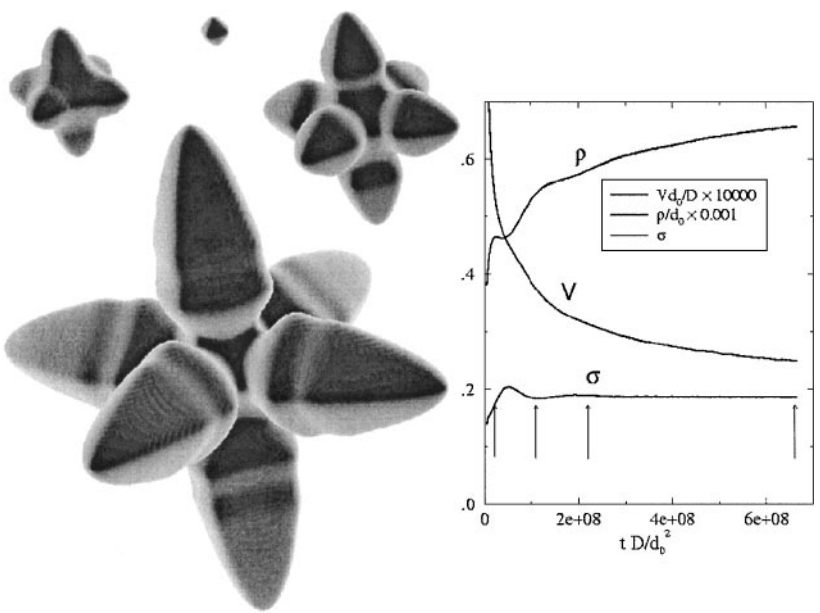

Figure 8 Three-dimensional dendritic growth simulation for a dimensionless supercooling of 0.05 and a 2.5% surface tension anisotropy. Snapshots of the structure are shown at the times corresponding to the arrows, and the diffusion field extends spatially on a much larger scale. The plot on the right side shows the evolution of the dimensionless tip velocity vd_0/D, tip radius ρ/d_0, and selection parameter $\sigma = 2Dd_0/\rho^2 v$, where d_0 is the capillary length, and D is the diffusion coefficient. This run took 6 h on 64 processors of the CRAY T3E at NERSC and is at the limit of what is computationally feasible.

boundary, with a uniform inlet velocity and temperature, and leaves through the bottom boundary (44, 45). The dendrite tip pointing toward the top boundary into the flow grows at a much faster velocity than the three other tips. The predicted heat transport enhancement owing to the flow at the upstream growing dendrite tip is in quantitative agreement with a two-dimensional Ivantsov transport theory modified to account for convection (47) if a tip radius based on a parabolic fit is used (44). Furthermore, using this parabolic tip radius, the predicted ratio of selection parameters without and with flow is found to be close to unity, which is in agreement with linearized solvability theory (47) for the ranges of the parameters considered (44). Dendritic side branching in the presence of a forced flow has also been quantitatively studied (45). It has been shown that the asymmetric side branch growth on the upstream and downstream sides of a dendrite arm, growing at an angle with respect to the flow, can be explained by the differences in the mean shapes of the two sides of the arm.

If extended to three dimensions, such phase-field simulations could help to clarify the inconsistent results that experimental investigations have yielded on the effect of flow on the operating state of a dendrite tip. An example of a three-dimensional phase-field simulation of dendritic growth in the presence of a forced flow is shown in Figure 10 (Y. Lu, C. Beckermann & A. Karma, unpublished research). More detailed three-dimensional results with flow have recently been reported by Jeong et al. (46). Considerable advances in computational efficiency and resources are needed before three-dimensional simulations with flow can be performed for parameter ranges that are representative of actual experiments.

ALLOYS Although some phase-field simulations of coupled heat and solute transport during dendritic growth of a binary alloy have recently been reported (48), previous studies usually make some assumptions to treat the temperature without solving the heat equation, which allows for focusing on the phase field and solute diffusion equations. Three assumptions have been used: isothermal temperature (as in solution growth, effectively ignoring the latent heat), frozen temperature gradient (to simulate directional solidification), and time dependent but spatially uniform temperature (as in a recalescing system). These studies do not use the thin interface analysis for alloys recently developed by Karma (24).

Alloy results for isothermal growth are shown in Figure 11 (15). Such simulations were initiated with a small solid seed and a value of dimensionless supercooling of 0.86 (supercooling divided by the freezing range) and thermodynamics for a lens-shaped phase diagram. As for pure materials, simulations of dendritic growth for alloys exhibit quite realistic growth shapes. A dendrite tip radius is selected naturally from the solution to the differential equations. Simulations also show many other features common to real dendritic structures; e.g., secondary arm coarsening and microsegregation patterns. The local variation of the liquid composition as it relates to the local curvature is apparent in the mush, agreeing with that expected from the Gibbs-Thomson effect. Non-isothermal

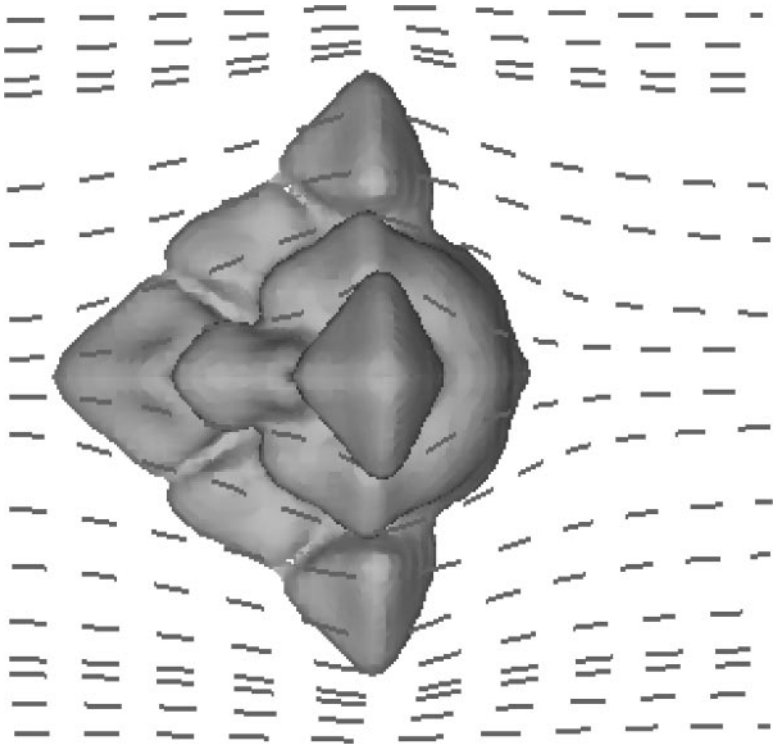

Figure 10 Three-dimensional simulation of free dendritic growth with fluid flow (Y. Lu, C. Beckermann & A. Karma, unpublished research). The melt enters at the left boundary, with a uniform inlet velocity and temperature, and leaves through the right boundary. The lines indicate the flow.

calculations using the frozen temperature gradient approximation can be found in References (23, 49).

In a recalescing system, for example (50), the temperature-time behavior is determined using a heat balance for a specified external heat extraction rate and the release of latent heat due to the increase in the amount of solid. Such simulations were performed for an initial value of dimensionless supercooling of 0.86. After the start of dendritic growth, recalescence occurs, and complete solidification is achieved at long times. Figure 12 describes the microsegregation obtained from simulations with heat extraction rates that would correspond to initial cooling rates of 1.7×10^4 K/s and 3.4×10^4 K/s. The microsegregation curves from the simulations were obtained by integration of histograms giving the number of pixels of the solid with concentrations in various bins. A description of the microsegregation using the assumptions of the Scheil method is shown for comparison.

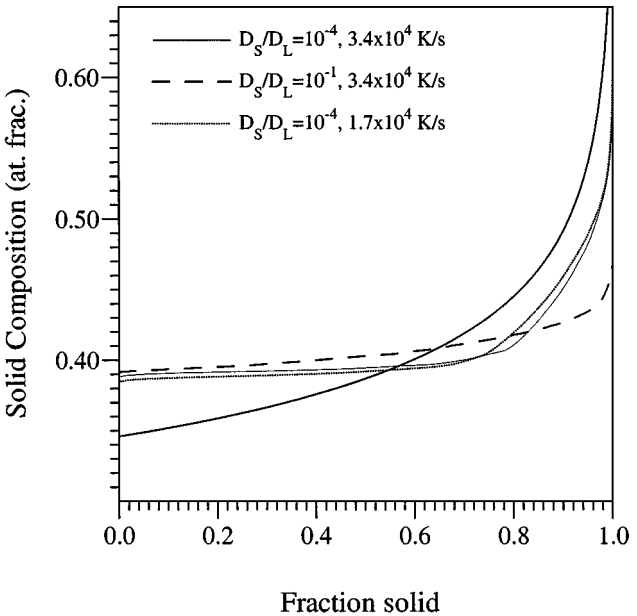

Figure 12 Microsegregation in alloy dendritic growth. Four microsegregation curves are shown: Two correspond to cooling rates of 3.4×10^4 and 1.7×10^4 K/s. The fourth curve shows the prediction of the Scheil model.

The concentration at zero fraction solid in Figure 12 represents the Cu concentration near the core of the dendritic tips. The simulated values are significantly higher than is predicted from the Scheil calculation. This effect is well known and is due to the kinetics of the dendrite tip from the supercooled melt. As the fraction solid increases, the solute profiles are quite flat compared with the Scheil prediction. This effect has been found experimentally for rapidly solidified alloys (51). One also notes that the difference between the two diffusion ratios, $D_S/D_L = 10^{-4}$ and 10^{-1}, follows the trend expected from various back diffusion models; i.e., that the final solid formed is higher in concentration if the solid diffusion is slow.

Eutectic Two-Phase Cell Formation

Eutectic two-phase cells, also known as eutectic colonies, are commonly observed during the solidification of ternary alloys when the composition is close to a binary eutectic valley. In analogy with the solidification cells formed in dilute binary alloys, colony formation is triggered by a morphological instability of the eutectic solidification front owing to solute diffusion in the liquid. The detailed mechanism of this instability has been investigated using a phase-field model of the directional solidification of a lamellar eutectic in the presence of a dilute ternary impurity (M. Plapp & A. Karma, unpublished research). This model was used to simulate

the formation of colonies starting from a planar lamellar front, as illustrated in Figure 13 (52). For equal volume fractions of the two solid phases, the simulations yielded good agreement with a recent linear stability analysis of a sharp-interface model (53), which predicts a destabilization of the front by long-wavelength modes that may be stationary or oscillatory. In contrast, for sufficiently off-eutectic compositions, the simulations revealed that the instability is initiated by localized two-phase fingers. In addition, simulations that focused on the dynamics of fully developed colonies showed that the large-scale envelope of the two-phase solidification front does not converge to a steady state, but exhibits cell elimination and tip-splitting events up to the largest times simulated. This example well illustrates the advantage of the phase-field approach over conventional front-tracking methods for modeling complex solidification morphologies in the presence of multiple phases and singular events such as lamellar termination and creation.

Coarsening and Flow

An example of phase-field simulations that have a direct bearing on modeling of mushy zones encountered in solidifying alloys has been provided by Diepers et al. (54). They modeled the coarsening (or ripening) of, and flow through, a solid-liquid mixture inside an adiabatic unit cell for an Al-4 wt% Cu alloy. Representative two-dimensional simulation results with and without flow are shown in Figure 14. The initial microstructure can be thought of as a cut through a stationary dendrite array inside a mushy zone.

The different curvature undercoolings of the various-sized solid particles in the unit cell lead to concentration gradients in the melt, causing the particles to exchange solute such that the larger particles grow at the expense of the smaller ones. The smaller particles eventually remelt completely, while the mean radius of the remaining particles increases with time (from left to right in Figure 14). At later times, several closely spaced particles coalesce. The phase-field simulations verified that in the long-time limit, in accordance with classical coarsening theories, the interfacial area decreases with the cube root of time in the case of no flow (upper panels in Figure 14).

In the simulation with flow (lower panels in Figure 14), a constant pressure drop was applied across the unit cell in the top-to-bottom direction. The coarsening causes the flow velocities to increase with time. This means that the decrease in the interfacial area because of coarsening results in an increase in the permeability of the microstructure. However, it is important to realize that the coarsening dynamics are influenced by convection. In other words, the microstructure of the mush not only governs the flow, but the flow also influences the evolution of the microstructure. The phase-field simulations revealed that in the long-time limit the interfacial area decreases with the square root of time in the presence of flow, as opposed to the cube root of time for purely diffusive transport. Diepers et al. determined the permeability from the phase-field simulations and found that the permeability normalized by the square of the interfacial area per unit solid volume

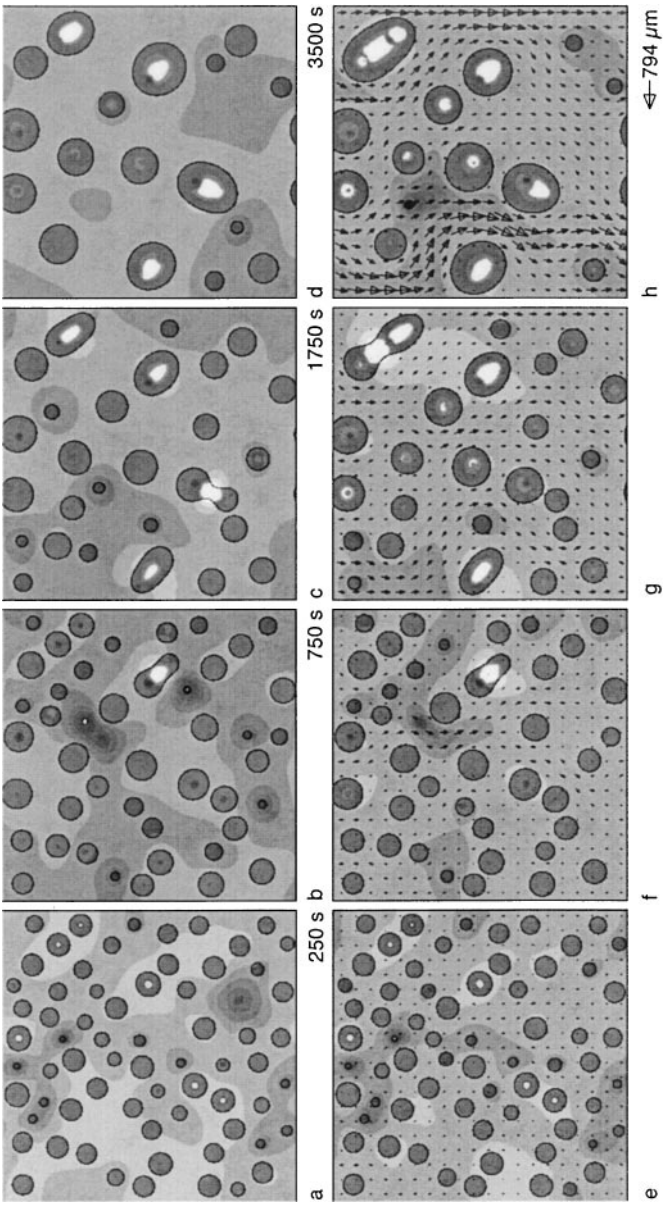

Figure 14 Phase-field simulation of coarsening of a solid-liquid mixture of an Al-4 wt% Cu alloy inside a periodic unit cell. The microstructure can be thought of as a two-dimensional cut through stationary dendrite arms inside a mushy zone of a solidifying alloy. The shading indicates solute concentration. Time increases from left to right. The upper panels are for purely diffusive transport. The lower panels are for a simulation with melt flow, where a constant pressure drop is applied in the top-to-bottom direction. The arrows indicate the liquid velocity.

is constant in time. By performing simulations with different volume fractions of solid inside the unit cell, they were able to correlate the permeability with the microstructural parameters present.

Bridging of Dendritic Sidearms

In alloys with a lens-type phase diagram or in alloys with a small, final fraction of eutectic, the side branches from adjacent primary trunks must join as the fraction of solid increases. The process of side branch bridging is often delayed until the late stages of solidification because of the requirement for rejected solute to leave the narrow region between adjacent arms. The bridging of side branches undoubtedly increases the tortuosity of the interconnected liquid, changing the permeability of the mushy zone and affecting porosity predictions. This process also changes the mechanical strength of the two-phase mixture, thus affecting the prediction of hot tearing tendency.

To gain a qualitative insight into this process, simulation of directional growth has been performed. Growth was initiated using seeds placed along one side of the computational domain. Due to computational limitations at the present time, these simulations were performed for growth into an isothermal supersaturated melt. A constant dendritic growth speed results, but there is no temperature gradient as would be present during directional solidification. Figure 15 shows a time sequence of images cut from a larger simulation. The position of the side branches, marked X and Y, are indicated in the larger simulation shown in Figure 16*a*. The frames are for a fixed location as the dendritic front moves through the region.

Although the calculations are for unrealistic interface thickness values and the system is two-dimensional, some details of the process are apparent. When two adjacent side branches collide with near-perfect alignment of their parabolic tips, bridging occurs quite rapidly at the tips. Solute can easily diffuse into the relatively broad region between tips. When they are misaligned, bridging is delayed and occurs farther behind the primary dendrite tips. Here the glancing collision of the two adjacent branches causes the formation of a long narrow liquid channel from which solute escape is more difficult. In three dimensions, the probability of aligned collisions would be more infrequent, delaying bridging until larger values of fraction solidify. We expect that much progress will be made in the near future on the problem of dendritic side branch bridging. Examination of the effect of interface thickness must be considered.

Dendrite Fragmentation During Reheating

Another important problem during solidification that involves a change in topology of dendrites is fragmentation. Such a process has been observed in transparent analogue systems subject to either extensive fluid flow or to a reversal of the thermal conditions during directional growth. The yield of dendrite fragments as a function of local variation in thermal and flow fields is an important quantity. When combined with an analysis of fragment survivability, it may lead to improved understanding of the columnar-to-equiaxed transition and to the formation of defects

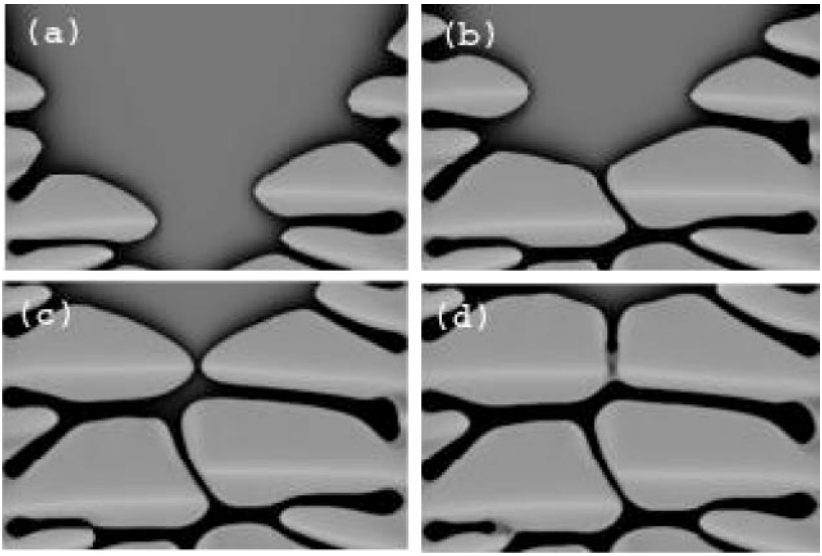

Figure 15 Sequence of simulations showing the time evolution of dendritic growth and bridging of side arms.

in directionally solidified single crystal superalloys. To gain some insight into this process, an isothermally grown structure was subjected to an instantaneous increase in the temperature from 1574 to 1589 K, changing the dimensionless supersaturation from 0.86 to 0.25 as shown in Figure 16. This rather severe thermal fluctuation caused the dendrites to quickly stop growing and partially remelt. Smaller increases in the temperature did not cause fragmentation. Nonetheless, the microstructure simulated during remelting is qualitatively close to that observed by Sato et al. (55).

The restriction of the present computations to two dimensions is the reason why such a large increase in temperature is required for fragmentation. Secondary arms are typically attached to the primary trunk by a thin-necked region. If one compares a peanut or dumbbell shape in two and three dimensions, the curvature near the neck region is always negative in two dimensions but can have either sign in three dimensions, depending on the exact geometry. Thus even during isothermal coarsening, a peanut shape in three dimensions can split in two. This is not possible in two dimensions where the shape will always circularize. Three-dimensional simulations are presently underway using parallel computing techniques.

A final point of discussion is found in the concentration profile in the solid near the melting interface. Due to the increase in temperature, the concentrations of the liquid and solid at the interface are both reduced (following the phase diagram lines) compared with the values present during growth. This reduction of the solid concentration at the interface is particularly evident in the narrow light region

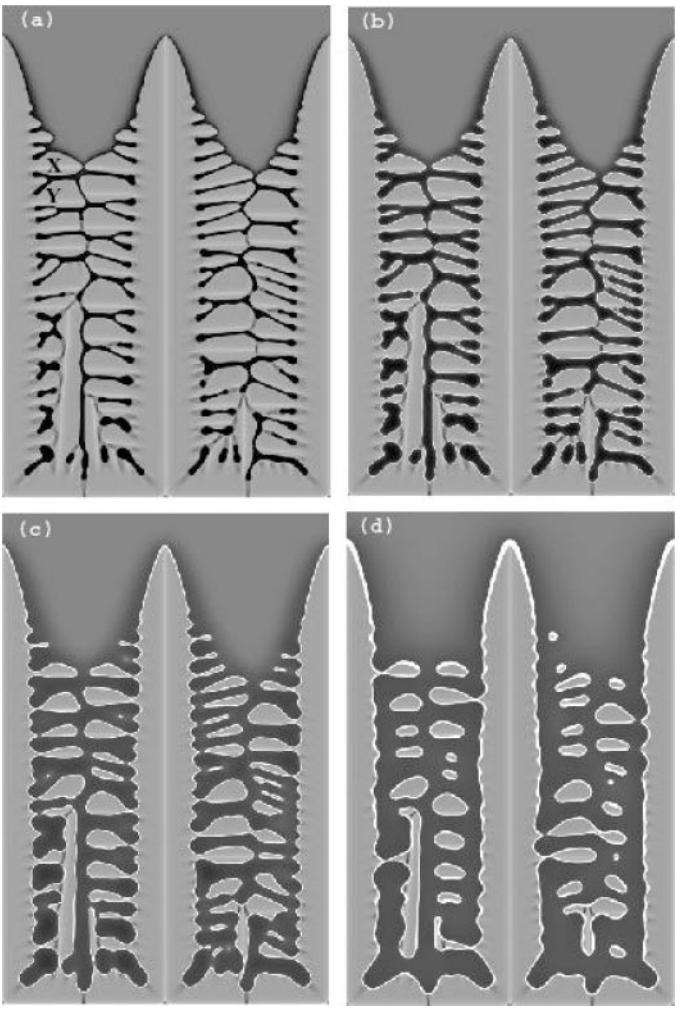

Figure 16 Melting of dendritic structure and formation of fragments when temperature is increased from the growth temperature of 1574 K shown in (*a*) to 1589 K shown at later times in (*b–d*).

in the solid that outlines the dendritic growth shape. Thus a sharp concentration gradient is induced in the melting solid.

Formation of Equiaxed Dendritic Grain Structure

To form an equiaxed grain structure, solid particles nucleate, grow, and impinge. Ideally, one should be able to describe this entire process within the same

thermodynamic model. There have been several attempts to use phase-field modeling to describe multigrain structures (11, 27), but here we focus on the model of Kobayashi et al. (29). Specifically, the free energy is changed according to the following rule:

$$F \rightarrow F + \int_V \left[s h_1(\phi) \, |\nabla\theta| + \frac{\varepsilon^2}{2} h_2(\phi) \, |\nabla\theta|^2 \right] dV, \qquad 45.$$

where θ is the local orientation of the crystal with respect to a lab frame. The functions h_1 and h_2 are monotonically decreasing functions of ϕ, which restrict the effect of misorientation to the solid. In addition to grain impingement during solidification, this model exhibits many features of classical models of grain boundary motion by curvature, as well as wetting transitions, and the possibility of microstructure evolution via grain rotation.

In Figure 17 we show several simulation snapshots that demonstrate the growth of three dendritic grains and their subsequent impingement. The calculation used an adaptive mesh, following the work of Tonhardt & Amberg (31). The secondary arms coalesce within each grain, but liquid remains at the grain boundaries because of both the build-up of solute between grains and the energy penalty of forming the grain boundary.

CONCLUSIONS

Compared with sharp-interface models of solidification, the phase-field method employs an extra field variable to describe whether a specific location is liquid or solid. The burden of this extra variable and its associated equation is offset by the avoidance of the mathematically difficult free-boundary problem for complicated interface shapes and the ability to handle topology changes. Realistic simulations of dendritic growth and other solidification microstructures can then be obtained using relatively simple numerical methods, although computing requirements can become excessive.

The examples of phase-field simulations of solidification presented here are no more than a snapshot of the many research activities currently underway in this field. The thermodynamic basis of phase-field models allows one to gain insight into the phenomenon of solute trapping during solidification. Simulations of dendritic growth of a pure substance have been used to verify microscopic solvability theory, both with and without flow in the melt. The solute pattern that forms in the solid during dendritic solidification has been computed for growth in a system at fixed temperature and in a system subject to recalescence through release of latent heat. These simulations were performed for relatively high initial supercoolings and/or cooling rates. Results presented for solidification of a eutectic alloy with a dilute ternary impurity illustrate the utility of the phase-field method for simulating multiphase and multicomponent systems. The phase-field method has also

been used to investigate some of the complex phenomena occurring inside mushy zones of solidifying alloys. The interplay between coarsening and flow has been simulated for a binary Al-Cu alloy, providing some insight into the evolution of the permeability of mushy zones. The bridging of dendritic side branches has been simulated and shown to be dependent on the geometry of the collision. Dendrite fragmentation during reheating of a previously solidified dendritic structure is shown, as well as the concentration profile present in a melting alloy dendrite. Finally, phase-field simulations of equiaxed dendritic growth illustrate the progress that has been made in predicting the multigrain structures typically found in castings.

Phase-field methods can have application to a broad class of materials problems. A recent non-exhaustive search of the literature revealed applications as diverse as voiding due to electromigration (56) and particle pushing at a liquid-solid interface (57).

ACKNOWLEDGMENTS

W.J.B. and J.A.W. express their gratitude to S.R. Coriell, J.W. Cahn, R. Kobayashi, G.B. McFadden, B.T. Murray, I. Loginova, and A.A. Wheeler. C.B. acknowledges support of his research by NASA under contracts NCC8-094 and NCC8-199. A.K. acknowledges support of US DOE grant DE-FG02–92ER45471.

The *Annual Review of Materials Research* is online at http://matsci.annualreviews.org

LITERATURE CITED

1. Lipton J, Glicksman ME, Kurz W. 1984. *Mater. Sci. Eng.* 65:57–63
2. Kurz W, Giovanola B, Trivedi R. 1986. *Acta Metall.* 34:823–30
3. Hunt JD. 1984. *Mater. Sci. Eng.* 65:75–83
4. Rappaz M. 1989. *Int. Mater. Rev.* 34:93–123
5. Brody HB, Flemings MC. 1966. *Trans. AIME* 263:615–24
6. Clyne TW, Kurz W. 1981. *Met. Trans. A* 12: 965–71
7. Mikheev LV, Chernov AA. 1991. *J. Cryst. Growth* 112:591–96
8. Harrowell PR, Oxtoby DW. 1987. *J. Chem. Phys.* 86:2932–42
9. Khachaturyan AG. 1996. *Philos. Mag. A* 74:3–14
10. Braun RJ, Cahn JW, McFadden GB, Rushmeier HE, Wheeler AA. 1997. *Acta Mater.* 46:1–12
11. Chen LQ. 1995. *Scripta Met. Mater.* 32:115–20
12. Wheeler AA, Boettinger WJ, McFadden GB. 1992. *Phys. Rev. A* 45:7424–39
13. Wheeler AA, Boettinger WJ, McFadden GB. 1993. *Phys. Rev. E* 47:1893–909
14. Boettinger WJ, Wheeler AA, Murray BT, McFadden GB. 1994. *Mater. Sci. Eng. A* 178:217–23
15. Warren JA, Boettinger WJ. 1995. *Acta Met. Mater.* 43:689–703
16. Calginalp G, Xie W. 1993. *Phys. Rev. E* 48:1897–909
17. Bi ZQ, Sekerka RF. 1998. *Physica A* 261: 95–106
18. Karma A, Rappel WJ. 1996. *Phys. Rev. E* 54:R3017–20

19. Kobayashi R. 1994. *Exper. Math.* 3:59–81
20. McFadden GB, Wheeler AA, Braun RJ, Coriell SR, Sekerka RF. 1993. *Phys. Rev. E* 48:2016–24
21. Elder KR, Drolet F, Kosterlitz JM, Grant M. 1994. *Phys. Rev. Lett.* 72:677–80
22. Provatas N, Goldenfeld N, Dantzig JA. 1998. *Phys. Rev. Lett.* 80:3308–11
23. Karma A, Lee YH, Plapp M. 2000. *Phys. Rev. E* 61:3996–4006
24. Karma A. 2001. *Phys. Rev. Lett.* 87:115701
25. Beckermann C, Diepers HJ, Steinbach I, Karma A, Tong X. 1999. *J. Comp. Phys.* 154:468–96
26. Wheeler AA, McFadden GB, Boettinger WJ. 1996. *Proc. R. Soc. London Ser. A* 452: 495–525
27. Steinbach I, Pezzolla F, Nestler B, Sesselberg M, Prieler R, Schmitz GJ, Rezende JLL. 1996. *Physica D* 94:135–47
28. Tiaden J, Nestler B, Diepers HJ, Steinbach I. 1998. *Physica D* 115:73–86
29. Kobayashi R, Warren JA, Carter C. 2000. *Physica D* 140:141–50
30. Nestler B, Wheeler AA. 2000. *Physica D* 138:114–33
31. Tonhardt R, Amberg G. 1998. *J. Cryst. Growth* 194:406–25
32. Tonhardt R, Amberg G. 2000. *J. Cryst. Growth* 213:161–87
33. Tonhardt R, Amberg G. 2000. *Phys. Rev. E* 62:828–36
34. Anderson DM, McFadden GB, Wheeler AA. 2000. *Physica D* 135:175–94
35. Ahmad NA, Wheeler AA, Boettinger WJ, McFadden GB. 1998. *Phys. Rev. E* 58: 3436–50
36. Aziz MJ. 1982. *J. Appl. Phys.* 53:1158–68
37. Aziz MJ. 1996. *Metall. Mater. Trans. A* 27: 671–86
38. Plapp M, Karma A. 2000. *Phys. Rev. Lett.* 84:1740–43
39. Bragard J, Karma A, Lee YH, Plapp M. 2002. *Interface Sci.* In press
40. Langer JS. 1986. *Phys. Rev. A* 33:435–41
41. Kessler DA, Levine H. 1986. *Phys. Rev. B* 33:7867–70
42. Hoyt JJ, Sadigh B, Asta M, Foiles SM. 1999. *Acta Mater.* 47:3181–87
43. Hoyt JJ, Asta M, Karma A. 2001. *Phys. Rev. Lett.* 86:5530–33
44. Tong X, Beckermann C, Karma A. 2000. *Phys. Rev. E* 61:R49–52
45. Tong X, Beckermann C, Karma A, Li Q. 2001. *Phys. Rev. E* 63:061601
46. Jeong JH, Goldenfeld N, Dantzig JA. 2001. *Phys. Rev. E* 64:041602
47. Bouissou P, Pelce P. 1989. *Phys. Rev. A* 40:6673–80
48. Loginova I, Amberg G, Agren J. 2001. *Acta Mater.* 49:573–81
49. Boettinger WJ, Warren JA. 1999. *J. Cryst. Growth* 200:583–91
50. Boettinger WJ, Warren JA. 1996. *Met. Mater. Trans. A* 27:657–69
51. Boettinger WJ, Bendersky LA, Coriell SR, Schaefer RJ, Biancaniello FS. 1987. *J. Cryst. Growth* 80:17–25
52. Karma A. 2001. In *Encyclopedia of Materials: Science and Technology*, ed. KHJ Buschow, RW Cahn, MC Flemings, B Ilschner, EJ Kramer, S Mahajan, pp. 6873–86. Oxford: Elsevier. Vol. 7
53. Plapp M, Karma A. 1999. *Phys. Rev. E* 60:6865–89
54. Diepers HJ, Beckermann C, Steinbach I. 1999. *Acta Mater.* 47:3663–78
55. Sato T, Kurz W, Ikawa K. 1987. *Trans. Jpn. Inst. Met.* 28:1012–21
56. Bhat DN, Kumar A, Bower AF. 2000. *J. Appl. Phys.* 87:1712–21
57. Ode M, Lee JS, Kim SG, Kim WT, Suzuki T. 2000. *ISI J. Int.* 40:153–60

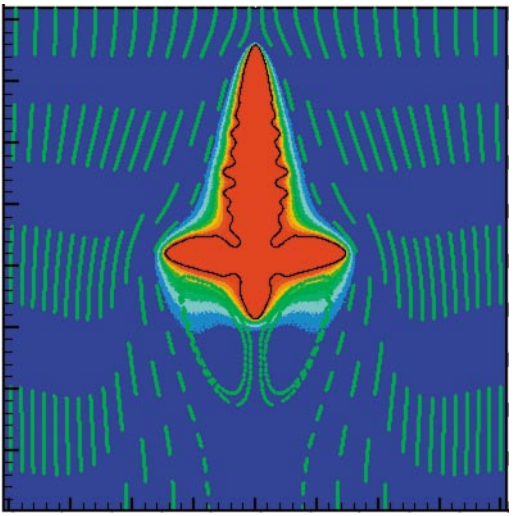

Figure 9 Two-dimensional simulation of free dendritic growth with fluid flow. The melt enters at the top boundary, with a uniform inlet velocity and temperature, and leaves through the bottom boundary. The *colors* indicate temperature and the *light lines* are the streamlines.

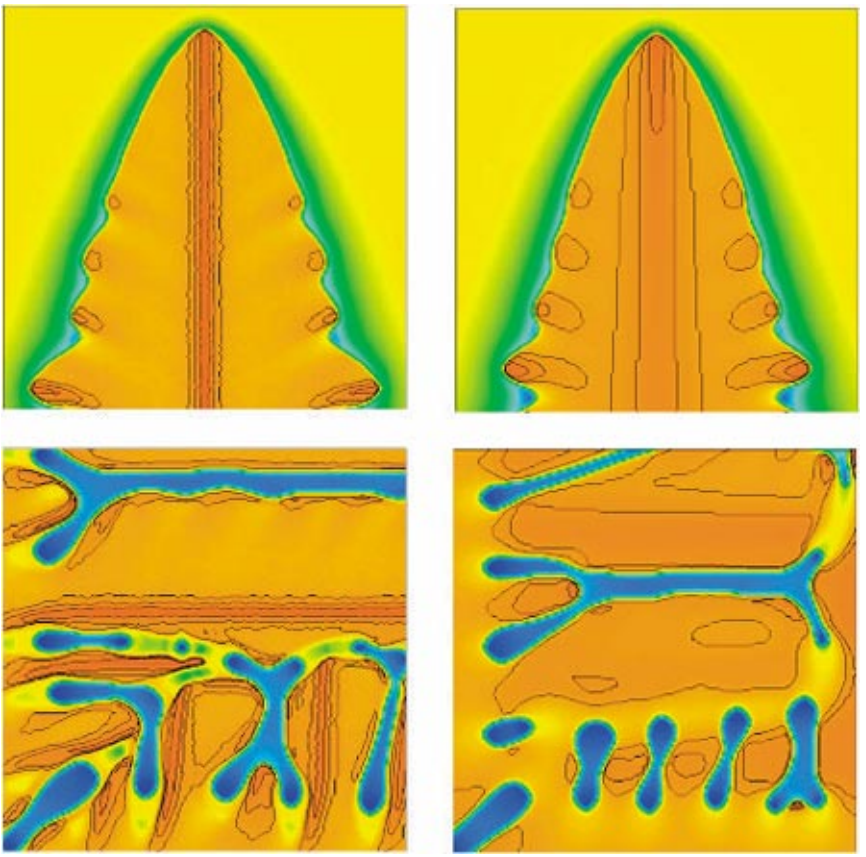

Figure 11 Morphologies and microsegregation patterns for isothermal alloy dendrite growth with a dimensionless supersaturation (undercooling) of 0.86. The *left and right panels* are for $D_S/D_L = 10^{-5}$ and 10^{1}, respectively. The *top pictures* show the tip region and the *bottom pictures* show a region deep in the mushy zone where liquid remains.

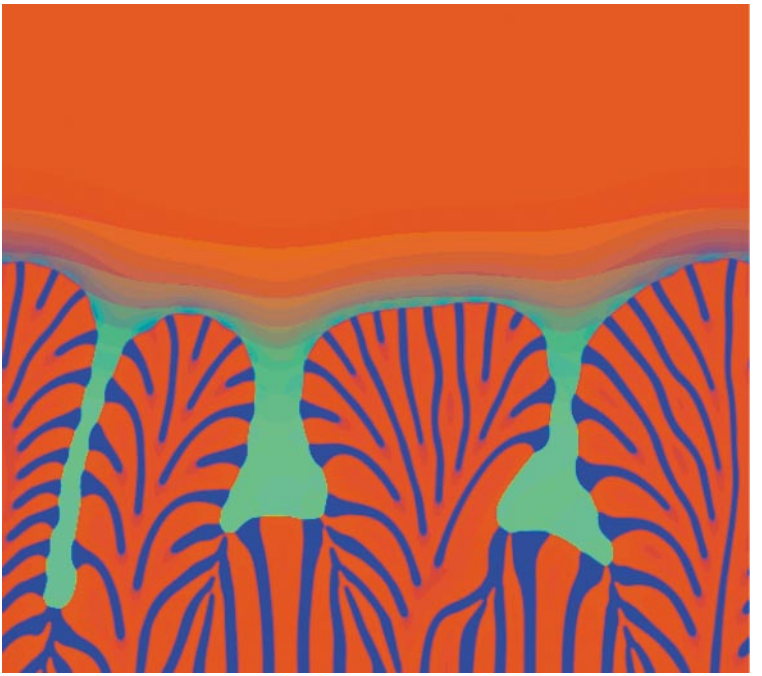

Figure 13 Snapshot of the late stage of two-phase cell formation subsequent to the morphological instability of a slightly perturbed eutectic interface in the presence of a dilute ternary impurity (M. Plapp & A. Karma, unpublished research).

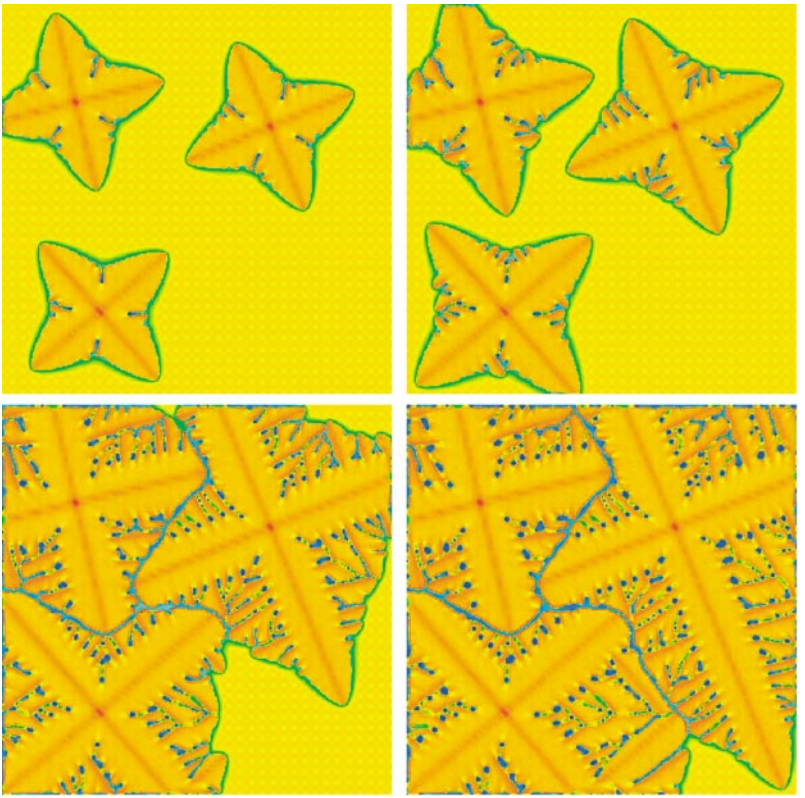

Figure 17 A phase-field simulation of alloy grain impingement (I. Loginova, Y. Wen & J.A. Warren, unpublished research). Three seeds were introduced into an undercooled melt under the same conditions as those of Figure 11. In the final picture, the secondary arms have coalesced within each grain, but liquid remains at the grain boundaries because of the build-up of solute between grains and the energy penalty of forming the grain boundary.